Lunar Surface Operation Testbed (LSOT)

Ashitey Trebi-Ollennu, Khaled S. Ali, Arturo L. Rankin, Kam S Tso, Christopher Assad, Jaret B Matthews,
Robert G Deen, Douglass A Alexander, Risaku Toda, Harish Manohara, Mohammad Mojarradi,
Michael Wolf, John R Wright, Jeng Yen, Frank Hartman, Robert G Bonitz, Allen R Sirota and Leon Alkalai

Jet Propulsion Laboratory, California Institute of Technology
4800 Oak Grove Dr.
Pasadena, CA 91109
818-354-8402
ashitey@jpl.nasa.gov

Abstract— This paper describes a high fidelity mission concept systems testbed at JPL, called Lunar Surface Operations Testbed (LSOT). LSOT provides a unique infrastructure that enables mission concept studies designers to configure and demonstrate end-to-end surface operations using existing JPL mission operations and ground support tools, Lander, robotic arm, stereo cameras, flight software, and soil simulant (regolith), in a high fidelity functional testbed. This paper will describe how LSOT was used to support the MoonRise mission concept study. MoonRise: Lunar South Pole-Aitken Basin Sample Return Mission would place a lander in a broad basin near the moon's South Pole and return approximately two pounds of lunar materials to Earth for study. MoonRise was one of three candidate missions competing to be selected as the third mission for NASA's New Frontiers Program of Solar System Explorations. LSOT was used to demonstrate JPL's extensive experience and understanding of the MoonRise Lander capabilities, design maturity, surface operations systems engineering issues, risks and challenges.

TABLE OF CONTENTS

1. INTRODUCTION

The Lunar Surface Operations Testbed (LSOT) provides a unique infrastructure with many "dials" that can be adjusted by mission concept studies systems engineers to evaluate how the performance of the system will be affected by key design parameters. LSOT also provides a platform for early risk reduction activities in Phase A of a NASA project life cycle. In addition, it provides a means to demonstrate end-to-end surface operations using existing JPL heritage mission operations and ground support tools, Lander, robotic arm, stereo cameras, flight software, and simulant (regolith), in a high fidelity functional testbed.

This paper will describe how LSOT was used to support the MoonRise mission concept study. MoonRise: Lunar South Pole-Aitken Basin Sample Return Mission would place a Lander in the interior of the giant South Pole-Aitken (SPA) basin located on the lunar far-side southern hemisphere [1,2]. The Lander would scoop, sieve, cache, and safely return to Earth a minimum of 1 kg of samples. Upon return to Earth, the samples would be examined and curated at NASA Johnson Space Center, analyzed in state-of-the-art laboratories, and made available for allocation to the science community. MoonRise was one of three candidate missions competing to be selected as the third mission for NASA's New Frontiers Program of Solar System Explorations. The proposed MoonRise Flight System would comprise two separate vehicles launched together on an Atlas V: the Communications Relay Satellite (ComSat) and the Sample Return Vehicle (SRV) and associated science payload. The SRV would consist of 4 modules representing different stages of the same vehicle: Sample Return Capsule (SRC), Lunar Ascent Module (LAM), Lunar Surface Module (LSM), and Lander Braking Module (LBM). The flight system payload would consist of MoonRise cameras — MoonRise Descent Imager (MDI), MoonRise Context Imager (MCI), and MoonRise Arm Camera (MAC) — and the Sample Acquisition and Transfer System (SATS).

The LSOT testbed configuration for MoonRise (shown in Figures 1 and 2) consisted of the Engineering Development Unit (EDU) of the Stardust Sample Return Capsule (SRC) (supplied by Lockheed Martin Aerospace), full size mockup of the Lunar Ascent Module (LAM), Lunar Surface Module (LSM), and Lunar Braking Module (LBM), a prototype MCI from the German Aerospace Center (DLR), MAC, prototype SATS Robotic Arm, End-Effector Scoop & Canister, Canister Capture System (CCS), and a sandbox with Lunar simulants including size distribution of rock fragments and rocks based on Apollo data [3]. The LSOT Command & Data Handling (C&DH) includes a PPC750 computer loaned from the Mars Exploration Rover (MER) project with command sequencing and telemetry functionality from MER, and COTS Payload Interface Module computers used to emulate the flight hardware interfaces and software drivers for the payload elements of the surface mission. The LSOT C&DH configuration for MoonRise enabled us to rapidly demonstrate end-to-end surface operations leveraging JPL heritage mission operations and ground support tools.

In the following sections we will provide a brief description of LSOT subsystems configuration for the MoonRise concept, present systems level end-to-end surface operations
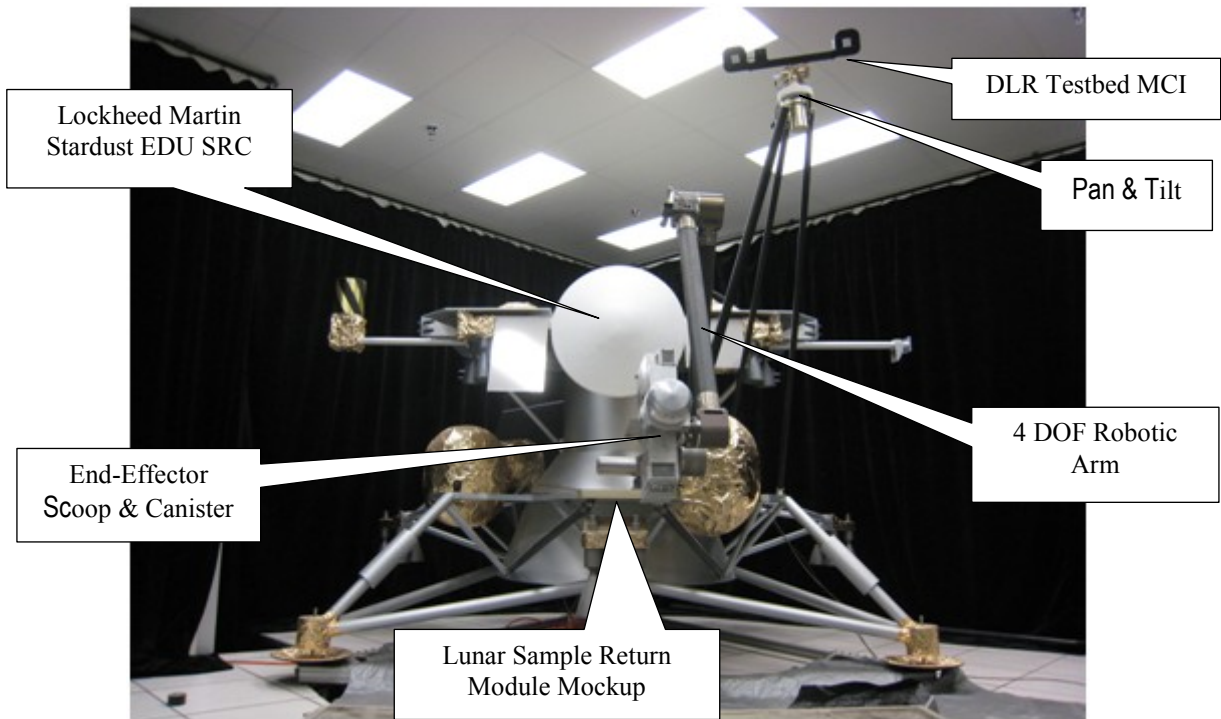
test results, and draw some conclusions.

Figure 1 - LSOT with Lunar Sample Return Module mockup, DLR Testbed MCI, COTS MAC, Robotic Arm, End-Effector (Scoop & Canister), Lunar Simulant Dig Bin, and Stardust EDU SRC.
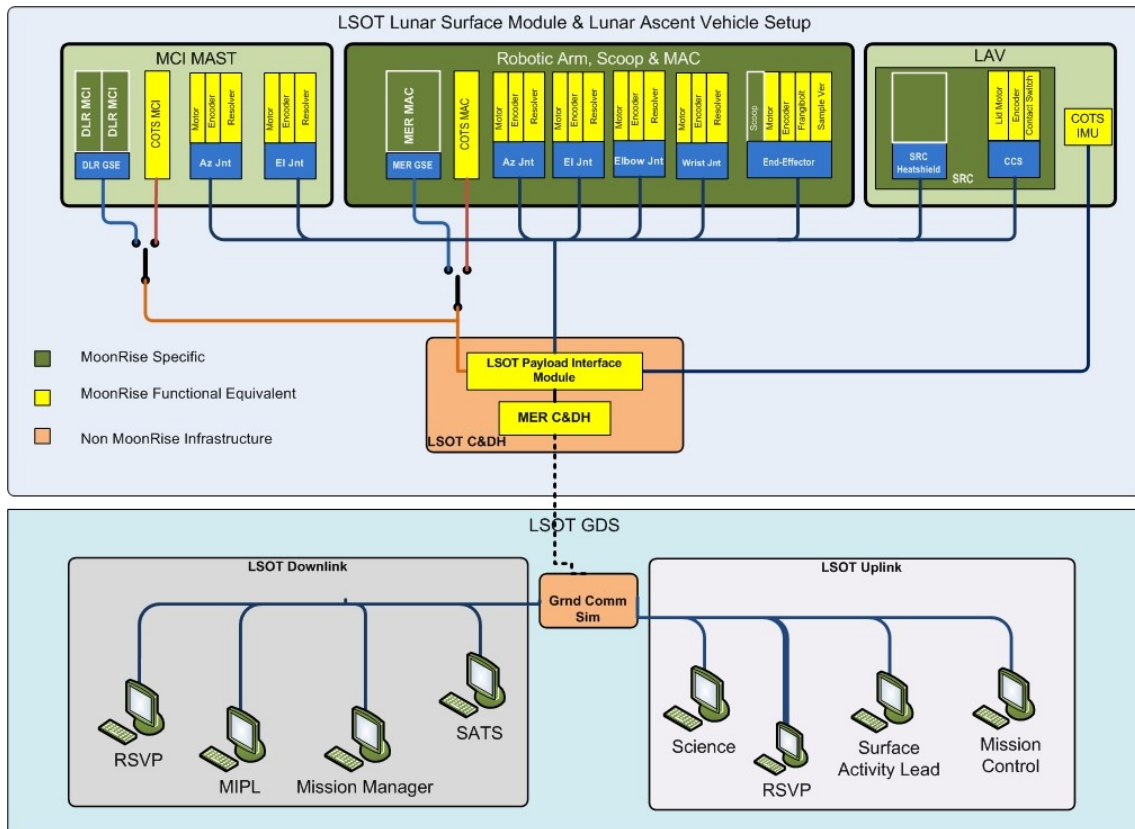

Figure 2 - LSOT MoonRise Concept Hardware Setup.

2. SYSTEM DESCRIPTION

MoonRise Prototype Context Imager

The MoonRise Context Imager (MCI) subsystem, shown in Figure 3, consists of a camera bar with a stereo pair of wide angle cameras (WACs) and one high resolution camera (HRC). It was designed and built by the German Aerospace Center, or Deutsches Zentrum für Luft und Raumfahrt (DLR). The design is based on the pancam under development for the proposed ExoMars rover mission baselined to launch in 2018 [4]. In the Moonrise testbed, the MCI was mounted on a pan-tilt unit atop the lander mast (see Figure 1). Design parameters for the MCI include overall mass of 1.8kg, power <= 8W, and operating temperature of -70 to 70 °C.

Figure 3 - The MCI testbed camera bar, with the right filter wheel cover removed. (DLR materials courtesy of: Ralf Jaumann, Nicole Schmitz, Frank Trauthan, DLR, Berlin)

The two WACs are mounted as a stereo pair with a baseline separation of 50 cm. Each WAC has a 34° diagonal field of view (FOV) with a fixed focus between 1.2m and infinity (Figure 4). The imager is a Cypress Fill Factory STAR1000 radiation hard CMOS image sensor, with 1024x1024 pixels at 15 μm pitch and a rolling shutter [5]. With this design the IFOV is 580μrad/pixel horizontal, giving a resolution of 1.2mm/pixel scale at 2m distance and 58mm/pixel scale at 100m. DLR designed interface circuits and programmed an FPGA board to control each imager and provide serial communication to the host computer system. Each camera is also equipped with a 12-position filter wheel for multispectral observations [4].

The HRC has a 1024 x 1024 pixel imager, with a 5° FOV and a mechanical autofocus capability between 0.9m and infinity. The IFOV is 83 μrad/pixel for a pixel scale of 0.17mm/pixel at 2m distance and 8.3mm/pixel at 100m (magnification factor ~7 compared to the WACs). The HRC was not used in the testbed experiments described here. Two software modules were written at JPL to control the camera pointing and image acquisition. The Mast module enables ground commands to move the pan and tilt axes to either absolute or relative angles in a user specified reference frame. It also includes an inverse kinematics model to point to a location in space specified by the user in Cartesian

coordinates in the Lander frame of reference. The camera software module initializes the cameras and provides commands to control image collection parameters and timing. It communicates through a TCP socket to a laptop running the MCI server software provided by DLR.
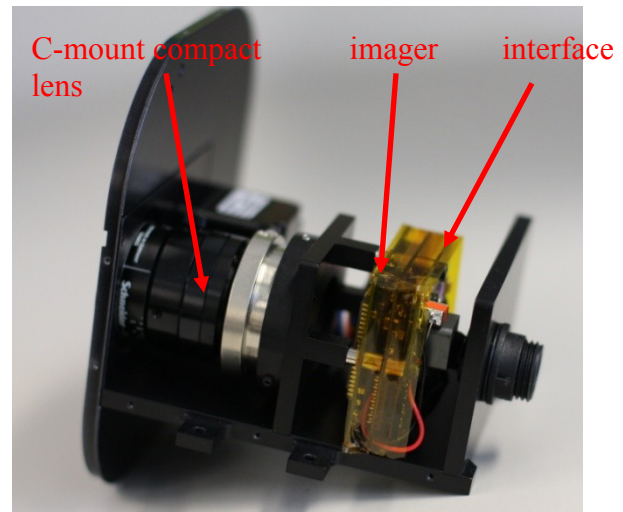

Figure 4 - WAC components.

Prototype SATS Robotic Arm

A custom four degree-of-freedom (yaw, pitch, pitch, pitch) arm was designed and built for the LSOT testbed. The arm was required to provide at least 230N of tip force for digging with 160% margin. The kinematics of this arm can be seen in the image below (Figure 5). The arm allows samples to be captured in the scoop and also places the sample canister in the Canister Capture System (CCS) on the Sample Return Capsule (SRC).

A cross-sectional view of the wrist joint can be seen in the Figure 6. This joint is representative of the basic actuator design throughout the arm. All of the joints are comprised of an 80:1 harmonic drive on the output driven by a 1.5:1 helical gear pass, then a multi-stage (3 or 4 stages) planetary gear and brushless DC motor.
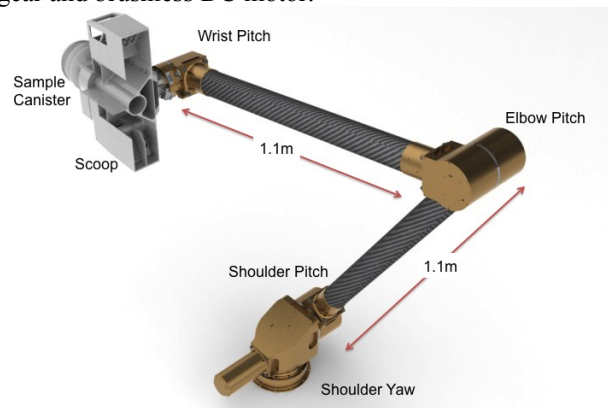

Figure 5 - The 4-DOF LSOT Robotic Arm.

All of the motors also have a safety brake (power to disengage) and incremental optical encoder on the input

side. There is also a single turn absolute optical encoder on the output of the joint. The encoder mount also serves as a grease trap for the helical pass lubrication.
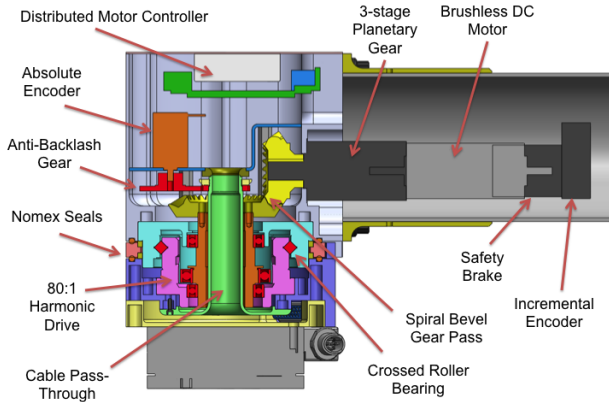

Figure 6 - Cross-Sectional View of the Wrist Pitch Joint.

The harmonic drive module includes an integrated crossed-roller bearing. This bearing was removed in the shoulder yaw joint and replaced with a higher moment capability X ball bearing. The joints all have Nomex felt seals for dust mitigation wherever relative rotation occurs. The structure of the arm is sized to take the ratchet torque of the harmonic drives. In this way, the harmonic drives act as mechanical fuses in the event of a severe overload event. The ratchet, max intermittent, and continuous torque and speed ratings for each joint are summarized in Table 1.

Moving hard-stops allow each joint to travel more than +/- 180° (see Figure 7). In order to encode the full range of motion with the single-turn absolute encoder, a slightly negative gear reduction is added between the joint output and the encoder. This gear pass includes an anti-backlash gear on the encoder. By comparing the output encoder values with the input encoder values, a crude measure of torque can be obtained [6]. This is achieved by characterizing the torsional stiffness in each joint, wherein the harmonic drive is the major source of deflection.

Table 1: Robotic Arm Actuator Torque, Speed, and Power Characteristics:

Joint	Ratchet Torque (Nm)	Max Int. Torque (Nm)	Speed at Max Int. (rad/s)	Input Power at Max Int. (W)	Max Cont. Torque (Nm)	Speed at Max Cont. (rad/sec)	Input Power at Max Cont. (W)	Overall Reduction
Shoulder Yaw	880	395	0.148	83	217	0.149	46	12480:1
Shoulder Pitch	1800	892	.094	154	459	0.110	79	5920:1
Elbow Pitch	880	395	0.148	83	217	0.149	46	12480:1
Wrist Pitch	450	191	0.35	98	113	0.35	58	5280:1

For precise knowledge of the forces between the scoop and the terrain/CCS, a six-axis force-torque sensor has been included between the scoop and the wrist output.
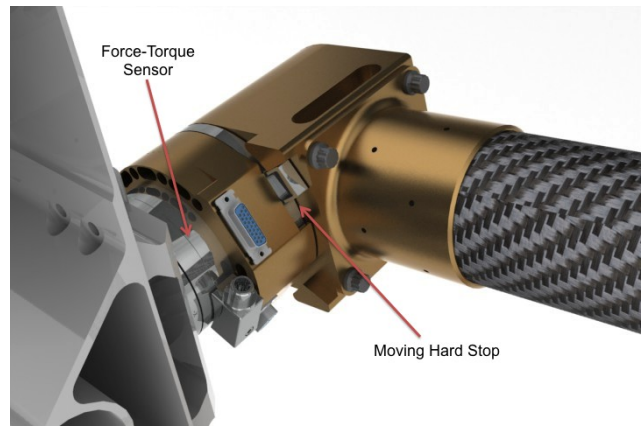

Figure 7 - The Wrist Pitch Joint with F-T Sensor and Moving Hard Stop.

Distributed motor controllers are used throughout the robotic arm and each controller is co-located with its associated joint. Distributed control significantly reduces the bulk diameter of wire harness traveling down the arm. The center of both the harmonic drive and the helical output gear are hollow, allowing for the harness to pass coaxially through without risk of chopping. This scheme greatly reduces the complexity of hardware required to protect the wire harness. Typical space robotic arms have relied on ribbon flex cable and spiral service loops to achieve the desired range of motion on the joint. This design is more consistent with industrial robotic arm design and allows for the use of a traditional round-wire harness, which is significantly less expensive and much easier to install/repair.

Sample Verification Sensor (SVS)

The sample verification sensor (SVS) is an in-situ sensor that measures the sample mass during sample acquisition. It would enable the spacecraft (or operator) to validate that sufficient material has been collected before launching the Lunar Ascent Module (LAM), with the Sample Return Capsule (SRC). The primary design criteria for the SVS are as follows: (i) the sensor should be integrated with the sample canister for robustness and ease of operation, (ii) the SVS must not contaminate the planetary sample, that is, should never come in physical contact with the sample, (iii) the integrated SVS should be lightweight, occupy a small volume and be shock tolerant to endure launch from the Moon and entry, descent and landing on Earth, (iv) the SVS should be robust to large temperature changes that may exceed 100 Kelvin during a Lunar day, and finally, (v) the SVS should be capable of measuring approximately 200–1000 grams of sample in lunar gravity to within 15% error.

SVS Hardware

Figure 8 shows a cross-sectional view of the sample mass sensor as it is mounted at the bottom part of a sample canister [7, 8].
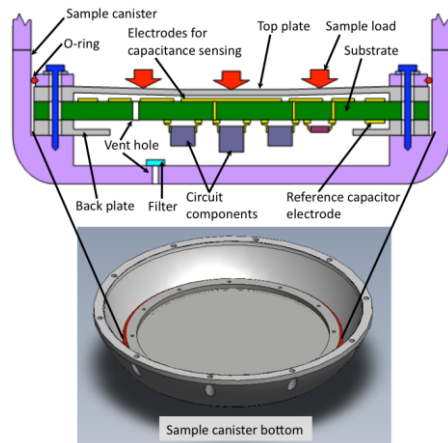
4

Figure 8 - Cross-sectional view of planetary sample mass sensor mounted at bottom of sample canister.

Figure 9 - Wide range sensing by distributed capacitors. (Not to scale)

Only the bottom section of sample canister is shown in Figure 8. The sensor is placed as a false-bottom so that the mass of the planetary sample is measured as part of the sample acquisition process. The SVS is constructed from stainless steel SUS304 and Aluminum 6061 alloy, as these materials have been previously approved for planetary sample handling applications. The top plate is a thin stainless steel SUS304 membrane that will deform under the sample load. The middle layer is a rigid substrate that has an array of electrodes on the top. There is a narrow gap between the SUS304 top plate and the substrate allowing the deformation of the top plate to be capacitively detected. Integrated circuits and other discrete components for the capacitance readout are mounted on the backside of the substrate. There is an additional back plate just under the substrate. The shape of the two plates (top and bottom) is identical except that the bottom plate has a center hole to allow tall circuit components protrusion. The SUS304 back plate is used as a reference capacitance for calibration purposes. The stack of top plate, substrate and bottom plate is attached to the bottom of canister by an Aluminum 6061 retainer ring and pressure-loaded fasteners. Small gaps on the mounting hole absorb coefficient of thermal expansion (CTE) mismatch when the sensor is exposed to large temperature change. An O-ring placed on the side of the retainer ring prevent small planetary sample particles from falling into narrow gaps on the edges of plates and substrate as this may cause sample contamination. Air vent holes equalize the cavity pressure to the ambient pressure. A microporous filter is placed on the vent hole so that dust particles will not interfere with capacitive measurement.

The deformation of the SUS304 top plate is illustrated in Figure 9. Assuming a light and uniform loading (Figure 9-B), the deformation is relatively large at the center of membrane compared to the outside. Therefore, capacitance at the center (C_{ctr}) shows a larger increase compared to the capacitance at the outside (C_{out}). When the applied load increases, the center portion of the membrane may touch the floor (Figure 9-C).
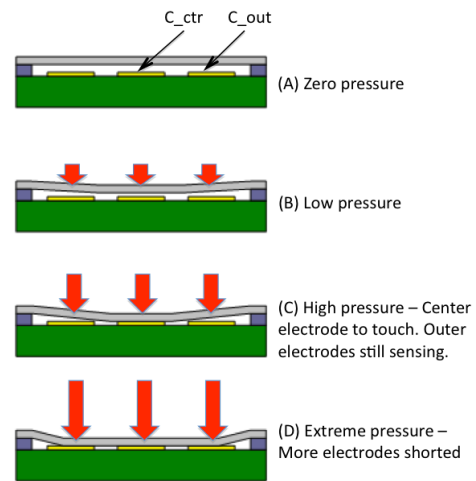
The C_{ctr} is then shorted and becomes unable to measure, but the outside C_{out} is still available. Using a series of concentric distributed capacitors expands the overall pressure measurement range. Figure 9-D shows the membrane experiencing extremely high load. In this case, the membrane is mostly touching and stopped at the underlying substrate and the capacitive readout is not functional. However, the membrane does not rupture easily because its mechanical strength is significantly reinforced by the underlying rigid substrate that prevents excessive strain. Therefore, the sensor can be made highly sensitive but robust against possible shocks that may be expected during launch and landing phases.

Based on a finite element analysis results, capacitance of these channels is estimated and plotted in Figure 10. The gap width is set to 100 μm and the load is applied uniformly. Due to the symmetry, channels 5, 6 and 7 results are omitted because they are identical to channels 3, 2 and 1, respectively. The center channel 4 ramps up the quickest and the capacitor becomes shorted at about 100 gram load when the top plate and electrode are in contact.
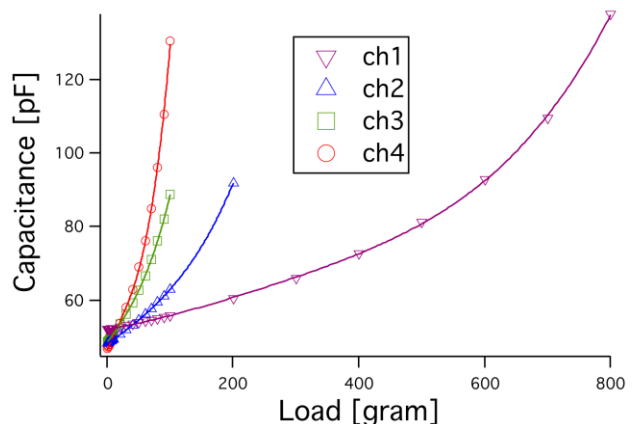

Figure 10 - Change of capacitance. (FEM simulation)

The outer electrodes ramp up relatively slowly and channel 1 can measure 800 grams loading or above. Therefore, inner

electrodes have higher sensitivity for a small loading range while outer electrodes have relatively low sensitivity over a wide range.
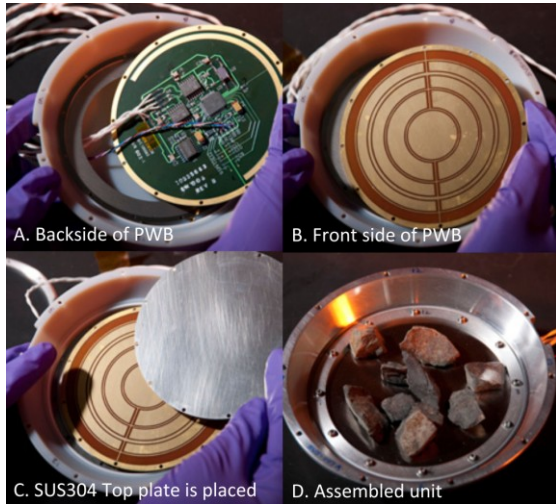

Figure 11 - Assembly steps of a sample mass sensor.

The assembly steps of the SVS mass sensor prototype are shown in Figure 11. Figure 11-A is the backside of a polyimide printed wiring board (PWB), which contains several ICs and discrete components. Capacitance reading circuitry on the backside of PWB transmits data to the host computer via a low-voltage differential signaling (LVDS) interface. The C-shaped electrode at near the edge on the substrate is used as a reference capacitor measurement. Figure 4B shows the top side of the PWB that contain seven concentric electrodes. In Figure 11-C, a 200 μm SUS304 top plate is placed on the PWB. Figure 11-D shows an assembled unit with simulated planetary rock samples.

SVS Estimation Algorithm

The SVS requires a technique to estimate the mass of the sample inside the canister, based on the capacitances of the seven SVS channels. The mass estimation algorithm reported here addresses both the calibration of each SVS channel and also the process for combining the capacitances read from each of the seven channels into a single mass estimate [9]. The exact loading distribution on the SVS membrane will vary from sample to sample and the membrane's deformation under similar masses can differ. Therefore, we take a probabilistic approach to the calibration of each SVS channel.

For the calibration phase, SVS capacitance data are collected for known masses under a variety of possible loading scenarios, though in all cases the distribution of sample within the canister is expected to be approximately uniform. A capacitance-vs.-mass curve is fit to this data for each of the seven channels. Moreover, we use the variance of these data to estimate a Gaussian probability distribution function (PDF) of the capacitance that may be read for a given sample mass, along a range of "reference masses".

For the mass estimation phase, the capacitance on each channel is observed. The curve fit of each channel provides a mass estimate "vote" for each channel—more formally, the curve fit value is interpreted as a mean μ_i of a probability distribution on the mass, conditioned on the ith channel's capacitance reading. To blend these seven estimates, we combine the seven PDFs into a single Gaussian distribution function, essentially taking the final estimate as an average of the estimates of the seven channels, weighted by the inverse of the channel's variance σ_i [9]. The final result is both the final mean (i.e., estimated mass) and the variance of our estimate. A complication arises when one or more channels short, which can occur when heavy loads deform the top SVS plate so much that it contacts the electrodes. This occurrence provides additional information to the mass estimation algorithm, as it indicates a certain "minimum mass" must be present in order to effect such a deformation. Two adjustments are made to account for the possibility of shorting channels: (a) a minimum likely mass is included in the mass estimate, and (b) different capacitance–mass curve fits are constructed for different regions (short vs. no short), as the membrane's deformation changes radically once it has contacted the electrode.

SVS Mass Measurement Results

Figure 12 shows a plot of a sample mass measurement experiment. Simulated planetary rock samples of known mass are poured over the SVS membrane in the sample canister, the capacitances observed, and the mass estimation algorithm run. Each sample mass is measured five times, which redistribution of the sample in between each measurement (shaking the canister by hand). As shown in Figure 12, the error percentage is very small when the sample mass is above 200 gram. On the other hand, the error percentage is relatively large when the sample mass is smaller. This can be explained by the fact that the small quantity samples tend to apply uneven pressure to the membrane depending on their location on the membrane. Large quantity samples tend to spread out evenly on the membrane and therefore apply relatively uniform pressure to the membrane.
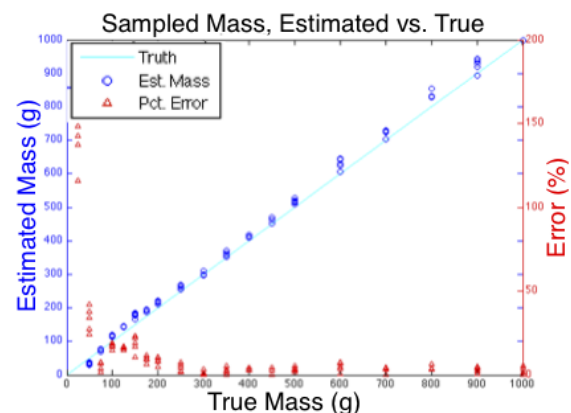

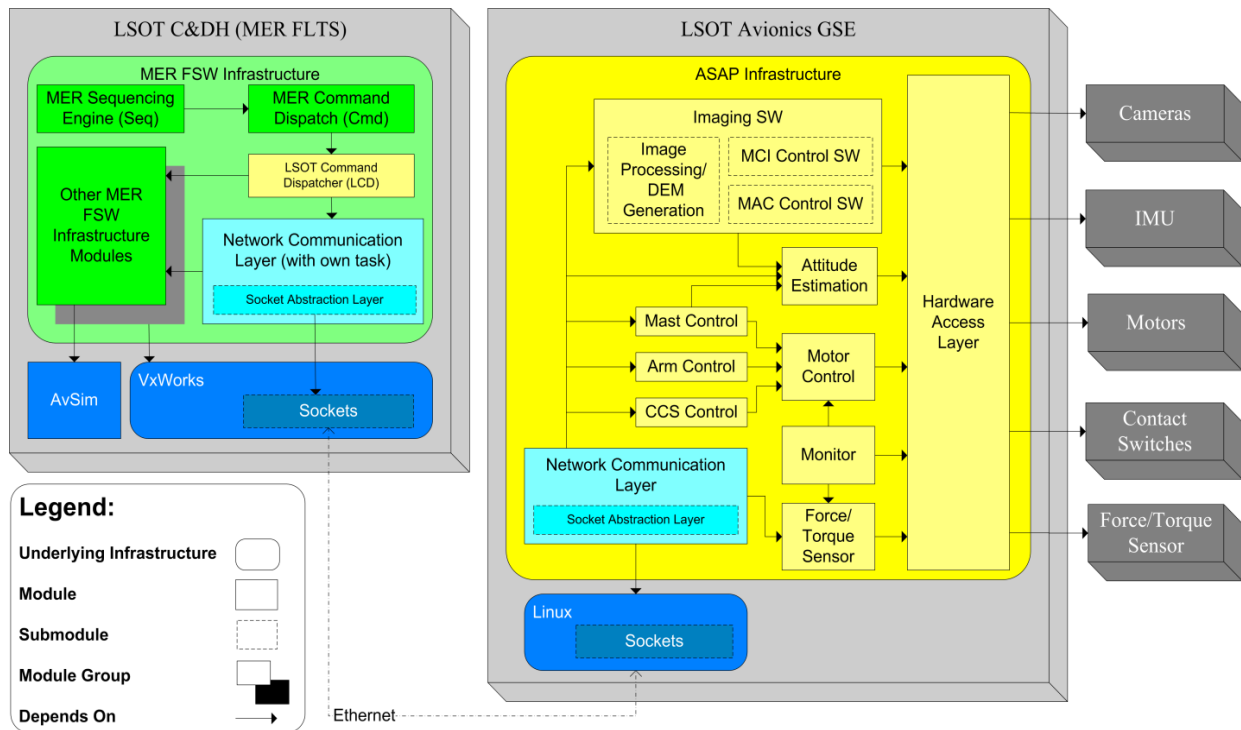**Figure 12 - Sample mass measured on prototype sensor.**

Figure 13 - LSOT onboard software architecture. A combined module-allocation view type. Modules colored light-yellow and light-blue were new for LSOT.

Software Architecture

As previously discussed, the software running onboard the vehicle is split between two physical computers, the Command and Data Handling (C&DH) machine and the Payload Interface Machine (PIM). Figure 13 shows the distribution of software between the two machines, as well as the breakdown of the software into modules. The application-level software on each machine runs on top of an existing heritage architecture. The inter-computer communication is handled via sockets.

C&DH Software Architecture

The LSOT C&DH is a Flight-Like Test Set (FLTS) borrowed from the NASA Mars Exploration Rover (MER) mission. This test set has a PPC750 processor running the VxWorks operating system and a version of the MER flight software (FSW) [10] which has been modified for LSOT. Additionally, another processor runs AvSim, a software simulation of the MER hardware, to simulate the MER hardware which is not present in the LSOT. The C&DH portion of the LSOT onboard software takes advantage of the MER FSW sequencing engine and command dispatcher. The MER sequencing engine provides a relatively rich language for sequence control and the capability to run multiple sequences in parallel. The LSOT Command Dispatcher (LCD) was added, containing command handlers to accommodate the new commands for the payload. These command handlers marshal the command and its arguments, and then request that the Network Communication Layer

(NCL) send the command to the PIM. The NCL saves the details of the request and then sends the command across a socket interface to the Network Communication Layer on the PIM. When a response is received from the PIM, the NCL replies to the LCD, which in turn replies to the MER FSW command dispatcher and sequencing engine.

PIM Software Architecture

The PIM runs the Linux operating system and the majority of the LSOT onboard software. Several application modules specific to the LSOT domain are built on top of the ATHLETE Software Architecture Platform (ASAP). ASAP is a distillation of the core infrastructure from the ATHLETE software [11]. While not actual flight software, the ATHLETE and ASAP software was heavily influenced by the MER flight software, and they borrow concepts which are key to the MER architecture.

For LSOT, a set of application modules have been added, running on top of the ASAP infrastructure. These modules include software to control and monitor the hardware, including the arm, mast, Canister Capture System (CCS), IMU, Force/Torque Sensor, contact switches, and cameras. Also, there are application modules to determine the lander attitude, process the images, and facilitate communication with the C&DH machine.

The Network Communication Layer (NCL) on the PIM handles communication with the C&DH machine. It

receives messages over the socket from the C&DH, unmarshals the messages, and dispatches the commands to the appropriate application module. Then, when it receives a response from the application module, the NCL creates and sends the appropriate response back to the C&DH.

On-Board Digability Assessment

Not all lunar terrain regions will be equally suitable for sample acquisition. For example, digging in regions containing large rocks would be less preferable to digging on level soil since there would be a higher risk of failure to collect the desired amount of sample for return to Earth. To determine the level of risk in digging in each region in the arm's workspace, we perform on-board digability analysis. On-board digability assessment is accomplished by executing a workspace panorama command sequence. There are three stages to the workspace panorama command sequence. First, twelve stereo pairs of Moonrise Context Imager (MCI) images are acquired of the arm workspace. Second, the perimeter points of 22 candidate dig sectors are generated. Finally, the digability of each candidate dig sector is assessed.

The twelve stereo pairs of WAC images in the workspace panorama are acquired in two tiers, six images per tier. The mast elevation angle for the top and bottom tier are 50° and 70°, respectively, with mast azimuth angles at 20° intervals for both tier. WAC images are saved in the same format as the MER navigation cameras (Navcams) [12].

The 3D perimeter points of the candidate dig sectors are generated using configurable parameters. The primary parameters are the minimum and maximum arm reach, the minimum and maximum arm azimuth, a dig swath width, and the number of radial segments in the workspace. A minimum and maximum arm reach of 1.14 and 2.27 meters, respectively, an arm azimuth span of 57.3°, a dig swath of 0.204 meters, and two radial segments results in 22 candidate dig sectors of approximately 20cm x 55cm.

Prior to evaluating the digability of each candidate dig sector, we generate a 3D reconstruction of the terrain using stereo ranging. The stereo pipeline includes image decimation (to 512x512 pixels), rectification, box pre-filtering, correlation, disparity gradient and region size post-filtering, and range generating stages [13]. One dimensional correlation is performed using five overlapping sum of absolute differences (SAD5) windows, the size of each window being 9x9 pixels. Processing the twelve stereo pairs of WAC images yields twelve stereo range images along with the intermediate stereo products including left rectified images. The twelve left rectified WAC workspace panorama images are illustrated in Figure 14.

The twelve left rectified and stereo range images are used to evaluate the dig goodness of each candidate dig sector based on a set of metrics. Currently, eight metrics are implemented: the maximum change in elevation difference in each sector, the elevation standard deviation in each sector, the forward and side tilt of each sector with respect to the payload frame, the maximum size of missing data regions in each sector, the percentage of a sector that has missing data, the roughness of each sector, and monochrome intensity standard deviation of each sector.

The elevation, tilt, and roughness analysis are performed using the twelve stereo range images, the monochrome intensity standard deviation analysis is performed using the twelve left rectified WAC images, and the missing data analysis is performed in map space. All of the range data that falls within a sector is used to generate a least squares plane fit of the sector. The forward and side tilt of a sector is the angle between the plane fit normal and the *yz* and *xz* payload frame planes, respectively. A 20cm resolution grid map, populated with the 12 stereo range images, is used to determine the maximum area and percentage of missing data within each sector.

Each of the 8 metrics forms a goodness image layer where the goodness value of each sector ranges from 0-1. Goodness values of 0 and 1 correspond to high and low risk, respectively. For each sector, the 8 goodness values are merged by selecting the lowest one. Including the merged goodness image layer, there are 9 goodness image layers for each of the 12 stereo pairs of WAC images for a total of 108 goodness images. Figure 15 illustrates the merged goodness images overlaid on the 3D terrain reconstruction for the twelve WAC images represented in Figure 14. The green sectors are safe for digging. The colors between green and red correspond to the increasing level of risk. In this example, the red regions contain rocks.

The data products generated by the workspace panorama command sequence are twelve raw left and right WAC images, twelve rectified left and right WAC images, twelve stereo disparity images, twelve stereo range images, 108 goodness images, and the 3D perimeter coordinates of each candidate dig sector. With a mast slew rate of 0.5°/s, and including a 1 second pause after each motion prior to imaging, the workspace panorama command sequence currently takes 3.5 minutes to execute. Of that time, the generation of dig sector perimeter points takes less than 0.5 seconds and the digability analysis and data product generation takes 21 seconds.

Figure 14 - Twelve left MCI images acquired by the workspace panorama command sequence. Two tiers of 6 images are acquired.
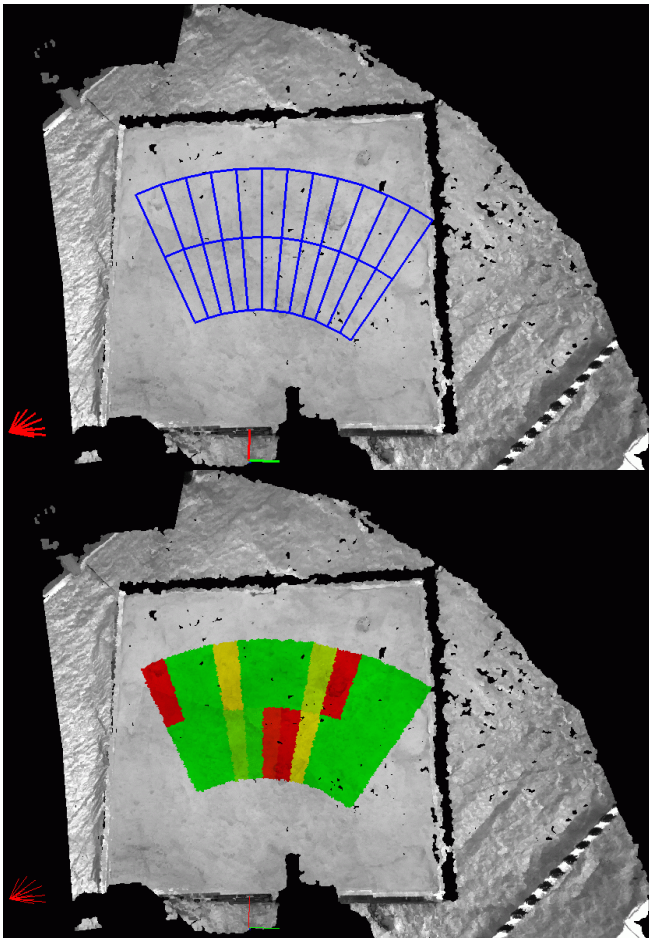
Figure 15 - The 3D stereo reconstruction of the workspace with a grid of 22 candidate dig sectors (top), and the corresponding digability goodness map (bottom). The red sectors contain surface rocks.

Mission Operations and Ground Data Tools

The Imaging Ground Data System (GDS) for LSOT, run by Multi-mission Image Processing Laboratory (MIPL), was a copy and subset of the Mars Exploration Rover (MER) system [14] with some minor modifications (see Figure 16). This system started with data products and created EDR's (Experiment Data Records), the raw image data. Then RDR's (Reduced Data Records) were generated, which includes results from processes like geometric rectification, stereo correlation, XYZ and surface normal generation, as well as retrieval of the LSOT goodness maps. Finally, mosaics and meshes were created as needed, and MIPL visualization tools were used to display the data.

Data from the testbed was packaged upstream into the same data product format as is used by MER. This allowed MIPL to use the MER telemetry processor (EDR generator) unmodified. The data products contained correctly-pointed camera models (calibration done by the LSOT team), which meant that the RDR generation programs also could be used unmodified. Although they are designed to be multimission - easily adaptable via subclasses for new missions [15] - this capability was not used for LSOT; the data looked exactly like MER data. However, a different spacecraft identifier (first letter of the filename) was used to avoid any chance of confusion. MER uses 1 for Opportunity, 2 for Spirit, and 4 for the testbed; LSOT used 3.

The execution of these programs, except for meshes and mosaics, was managed by the LSOT pipeline (Figure 16). This was a copy of the MER pipeline [16], with slight modifications. The modifications supported the different spacecraft ID and the use of day-of-year instead of Martian Sol number. In addition, several features not needed by LSOT were turned off.

A significant difference in LSOT compared to MER is the addition of "goodness maps", which provide a hazard assessment for each digging sector. These maps were generated onboard (see previous section) and downlinked; this was managed by a separate script. The product visualization tool "marsviewer" was modified to show these maps with appropriately-colored overlays.

Meshes were supported using specialized scripts derived from the MER pipeline. This is because the LSOT version of RSVP required a newer version of the mesh generation tool than is supported in MER. It is planned for this capability to be back-ported to MER in the future.

Mosaics were also generated via specialized scripts. For the Moonrise demo, two mosaics were created. The first was a vertical projection of the workspace, including an overlay of the goodness map (similarly mosaicked) (Figure 17). The second was a "people panorama" acquired during the demo showing the attendees (Figure 18). This simulated the science panorama in the Moonrise operations scenario.

For the purposes of the Moonrise demo, the stereo workspace imagery was acquired and processed shortly before the demo, for time reasons. The "people panorama" was acquired during the demo, as were images of the canister insertion process from both the mast camera (MCI) (Figures 20-22) and arm camera (MAC) (Figures 19 and 23). The products were displayed using the standard MIPL display tools "marsviewer" and "xvd".
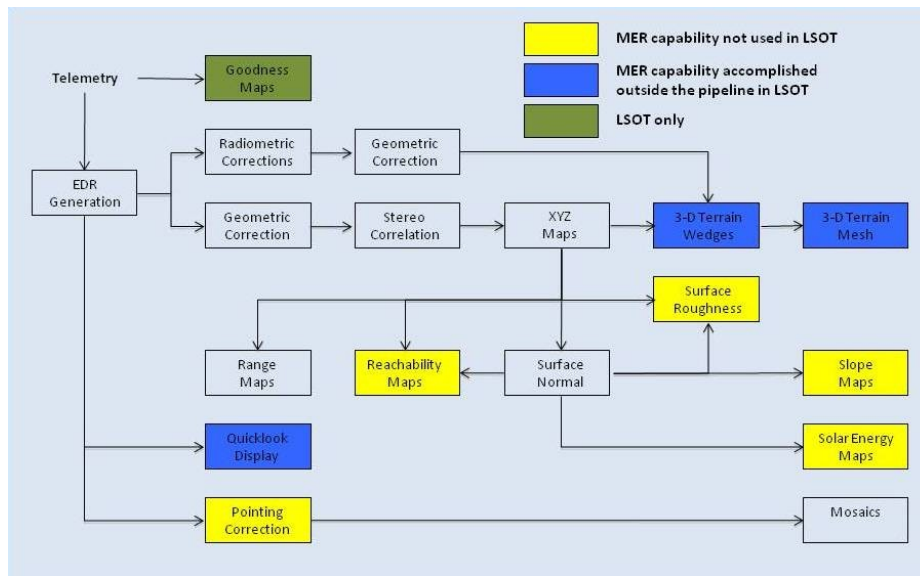
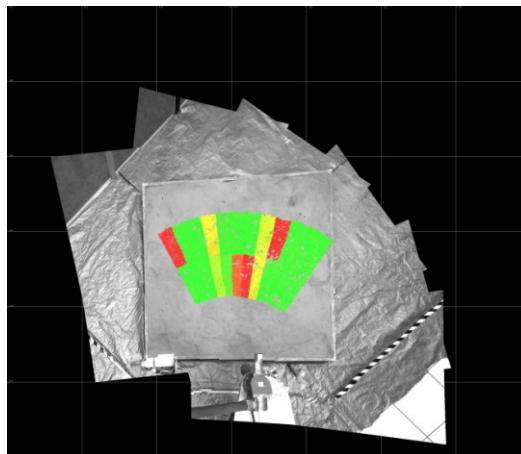**Figure 16 - MIPL Image Product Pipeline for LSOT**

Figure 17 - Workspace mosaic with goodness map overlay (green is best, red is worst)

Figure 18 - "People panorama", which simulated the Moonrise science panorama
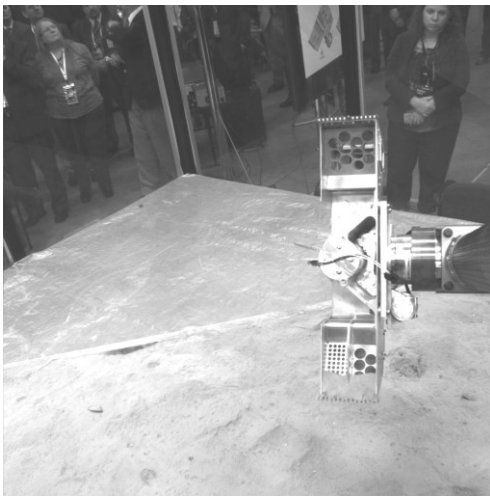
Figure 19 - View from the MAC showing simulated regolith in the scoop.
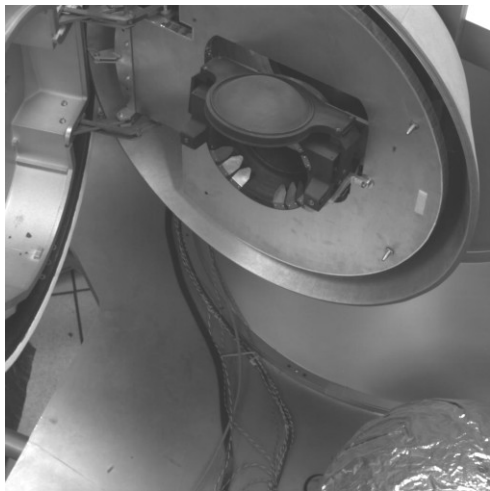

Figure 20 - View from the MCI showing the empty Canister Capture System (CCS), ready for insertion.
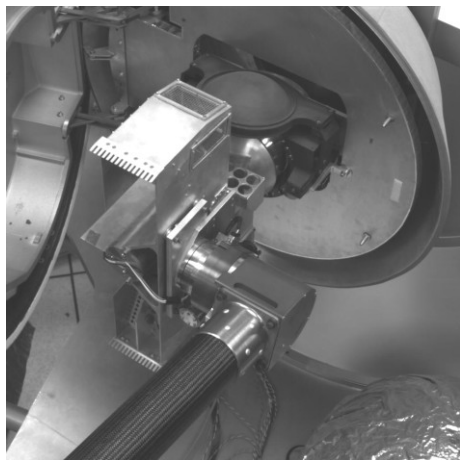

Figure 21 - View from the MCI showing the arm inserting the sample canister.
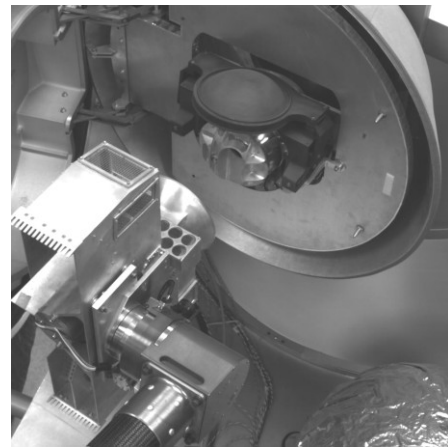

Figure 22 - View from the MCI showing the captured and released canister in the CCS.
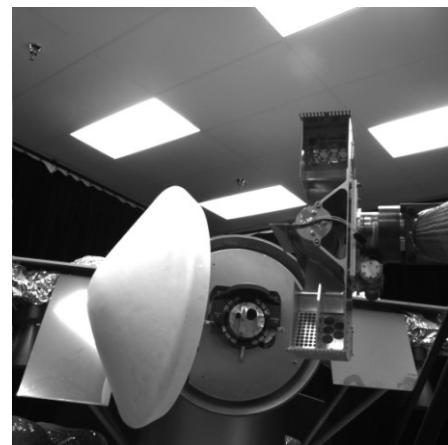

Figure 23 - View from the MAC showing the captured and released canister in the CCS.

LSOT Robot Sequencing and Visualization Program (RSVP)

The Robot Sequencing and Visualization Program (RSVP) [17] provides a high fidelity 3-D modeling and visualization tool, developed at JPL, for surface operations of rovers, landers, and in situ instruments. RSVP has been used for the Mars Pathfinder mission, MER, Phoenix and will be used for MSL surface operations. In addition, it is used for internal research activities such as the ATHLETE robot. The LSOT RSVP was configured using the MSL RSVP engine with minimum changes. Specific changes were to the 3D model of the spacecraft, the UI for the operator, and some code to connect the two. The following MoonRise concept spacecraft modules were incorporated into the 3D model: the Sample Return Capsule (SRC), Lunar Ascent Module (LAM), Lunar Surface Module (LSM), Lander Braking Module (LBM), MCI mast, robotic arm and end-effector, scoop, & canister as shown in Figures 24 and 25.

The RSVP tools include terrain model visualization and interaction, numeric data plotting and analysis, image display and interrogation, command sequence visualization, sequence rehearsal, kinematic modeling of spacecraft and

terrain interactions, and time-based modeling of spacecraft and planetary bodies for analysis of communication issues, incident solar energy, and shadowing. RVSP enables detailed simulation of the robotic arm motion, which is driven by the ground version of the ASAP software described earlier. LSOT command sequences were generated in RML using a component of RSVP, called the Robot Sequence Editor (RoSE), which provides text-oriented commanding for robotic arm, MCI and MAC. An additional component, HyperDrive, provides immersive 3-D graphical display to aid the sequence creation and review process. HyperDrive utilizes a combination of flight software and internal modules to perform command sequence execution, validation and playback. RSVP also supports the creation of documentation and archival products.

LSOT RSVP was used to simulate and visualize command sequences for sample acquisition, scooping, sieving, and transfer of the samples into the Sample Return Capsule.
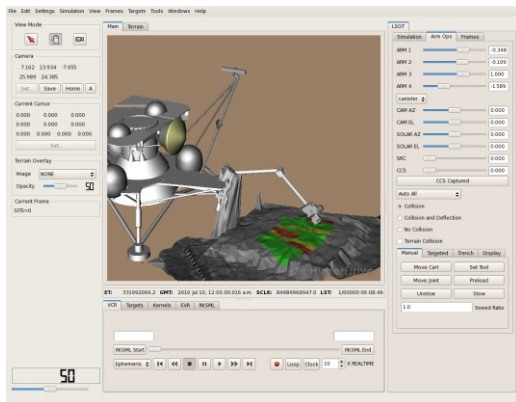

Figure 24 - LSOT RSVP Hyperdrive Window with digital elevation map and digability map overlay of the LSOT sandbox using images acquired by DLR Prototype MCI during the MoonRise site visit.
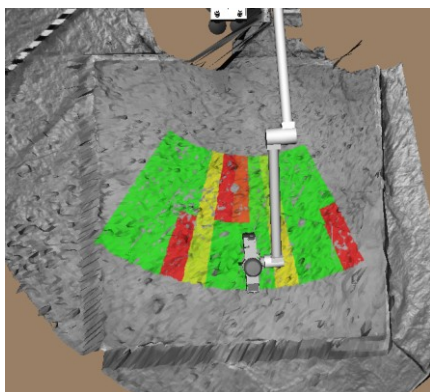

Figure 25 - A close up of LSOT RSVP Hyperdrive Window with digital elevation map and digability map overlay of the LSOT sandbox using images acquired by DLR Prototype MCI during the MoonRise site visit.

3. CONCLUSIONS

LSOT was used to demonstrate JPL's extensive experience and understanding of the proposed MoonRise lander capabilities, design maturity, surface operations systems engineering issues, risks and challenges. LSOT was used to demonstrate the end-to-end surfaces operations of the MoonRise mission concept study to the NASA reviewers' at a site visit in April 2011.

LSOT has demonstrated that a high fidelity testbed can be used as a platform for early risk reduction activities and to manage risks inherent in complex missions in Phase A of a NASA project life cycle. LSOT proved very useful in refining operational scenarios, validating operational timeline and margins, verification and staffing of operations including contingency operations planning. Employing high fidelity functional "dirty" testbeds with prototype hardware in Phase A of a NASA project life cycle can inform hardware design robustness issues and help define flight software and payload requirements, test nominal and fault timelines, and help establish preliminary system verification plans and better evaluate the maturity (TRL) of payload algorithms and hardware.

Currently, LSOT is being used in a similar capacity for a concept study for the GEophysical Monitoring Stations (GEMS) proposal to the NASA Science Mission Directorate (SMD) Discovery Program.

REFERENCES

[1] C. K. Shearer, B. L. Jolliff, L. Alkalai, D. A. Papanastassiou, P. Warren, and M. Wieczprek, "Sample Return from the Moon's South Pole-Aitken Basin (SPA): Enabling Solar System Class Science and Sample Return Missions to Other Destinations", Workshop on The Importance of Solar System Sample Return Missions to the Future of Planetary Science, The Woodlands Waterway Marriott Hotel , March 5-6, 2011, sponsored by NASA Planetary Science Division and Lunar and Planetary Institute

[2] B. L. Jolliff. , C. K. Shearer, D. A. Papanastassiou and L. Alkalai, "MOONRISE: South Pole-Aitken Basin Sample Return Mission for Solar Science", 2011 Annual Meeting of the Lunar Exploration Analysis Group

[3] W. D. Carrier, G. R. Olhoeft, and W. Mendell, Physical Properties of the Lunar Surface, Lunar Sourcebook, G. Heiken, D. Vaniman, and B. M. French, eds., Cambridge University Press,Cambridge, pp. 475-594, 1991.

[4] R. Jaumann, et al., 2007, The High Resolution Stereo Camera (HRSC) Experiment on Mars Express: Instrument Aspects and Experiment Conduct from Interplanetary Cruise through Nominal Mission, Planetary and Space Science, 55, 928-952, doi:10.1016/j.pss.2006.12003.

[5] http://www.onsemi.com/PowerSolutions/product.do?id=STAR1000

[6] C. Collins, "Stiffness Modeling and Force Distribution for the All-Terrain Hex-Limbed Extra-Terrestrial Explorer (ATHLETE)", Proc. ASME 2007 International Design Engineering Technical Conferences & Computers and Information in Engineering Conference, Las Vegas, Nevada, USA, September 4 – 7, 2007.

[7] JPL New Technology Report #47690.

[8] R. Toda, C. McKinney, S. P. Jackson, M. Mojarradi, A. Trebi-Ollennu and H. Manohara, "Development of Sample Verification Systems for Sample Return Missions", IEEE Aerospace Conference, Big Sky, MT, March 2011. doi:10.1109/AERO.2011.5747470

[9] JPL New Technology Report #48143

[10] Glenn Reeves, "Mars Exploration Rovers Flight Software", Waikoloa : IEEE Conference on Systems, Man and Cybernetics, 2005.

[11] Brian H. Wilcox, Todd Litwin, Jeff Biesiadecki, Jaret Matthews, Matt Heverly, Jack Morrison, Julie Townsend, Norman Ahmed, Al Sirota, Brian Cooper. "ATHLETE: A Cargo Handling and Manipulation Robot for the Moon.", Journal of Field Robotics, 2007, Vol. 24.

[12] D. Eisenman, C. Liebe, M. Maimone, M. Schwochert, and R. Willson, "Mars Exploration Rover Engineering Cameras," Sept 2001 SPIE Remote Sensing conference proceedings, Toulouse, France., September 2001.

[13] S. Goldberg, M. Maimone, and L. Matthies, "Stereo Vision and Rover Navigation Software for Planetary Exploration," March 2002 IEEE Aerospace conference proceedings, volume 5, Big Sky, Montana, USA, March 2002, 2025-2036.

[14] D. A. Alexander, et al. (2006), Processing of Mars Exploration Rover imagery for science and operations planning, J. Geophys. Res., 111, E02S02, doi:10.1029/2005JE002462.

[15] R. G. Deen, (2003), Cost savings through Multimission code reuse for Mars image products, paper presented at 5th International Symposium on Reducing the Cost of Spacecraft Ground Systems and Operations, Deep Space Commun. and Navig. Syst. Cent. of Excellence (DESCANSO), Jet Propul. Lab., Pasadena, Calif.

[16] D. Alexander, P. Zamani, R. Deen, P. Andres, and H. Mortensen (2005), Automated generation of image products for Mars Exploration Rover mission tactical operations, paper presented at 2005 International Conference on Systems, Man, and Cybernetics, Inst. of Electr. and Electron. Eng., Waikoloa, Hawaii.

[17] J. Wright, F. Hartman, B. Cooper, S. Maxwell, J. Yen, and J. Morrison, ''Driving on Mars with RSVP,'' IEEE Robot. Automat. Mag., vol. 13, no. 2, pp. 37–45, June 2006.

BIOGRAPHIES

AshiteyTrebi-Ollennu, FIET, FRAeS, SMIEE *is a technical group leader and robotics software engineer IV of the Mobility and Manipulation group at NASA Jet Propulsion Laboratory, California Institute of Technology, where he has been since 1999. He received his Ph.D. degree in control systems from Royal Military College of Science, Cranfield University, United Kingdom in 1996 and B.Eng. (Hons) from Queen Mary College, University of London, United Kingdom in 1991. Dr. Trebi-Ollennu received the 2008 NASA Exceptional Engineering Achievement Medal for his contributions to the Mars Exploration Rover mission, 2007 Outstanding Engineer Award from IEEE Region 6, 2007 Sir Monty Finniston Achievement Medal from Institution of Engineering and Technology, U.K., and 2010 Specialist Silver Award from the Royal Aeronautical Society, U.K. Dr. Trebi-Ollennu is a Fellow of the Institution of Engineering and Technology, U. K., and a Fellow of the Royal Aeronautical Society, U.K.*

Khaled S. Ali *received Master of Science and Doctor of Philosophy degrees, in 1995 and 1999, from the Georgia Institute of Technology in Computer Science. He received B.S. degrees in Computer Science and Mathematics from Vanderbilt University in 1992. Dr. Ali is a robotics software engineer at the NASA Jet Propulsion Laboratory. He is the Flight Software/Data Management Team Lead for the Mars Exploration Rover (MER) operations. He managed the development of the latest two versions of the MER flight software, which were uploaded in 2006 and 2009. Dr. Ali received the 2008 NASA Exceptional Achievement Medal for leadership and effective collaborative oversight of the technology infusion of new autonomy software into the MER flight software.*

Arturo L. Rankin *is a task manager and robotics software engineer III in the Surface Systems Perception Group at NASA Jet Propulsion Laboratory, California Institute of Technology, where he has been since 1997. He received a B.S. degree in Mechanical Engineering in 1987 from the Catholic University of America, Washington D.C., and M.S. and Ph.D. degrees in Mechanical Engineering in 1993 and 1997 from the University of Florida. Dr. Rankin has developed obstacle detection, terrain perception, and terrain mapping software for a variety of terrestrial and planetary projects. In 2005-2007, Dr. Rankin led an effort that successfully integrated the Field D* global path planner into Mars Exploration Rover flight software.*

Kam S Tso *received his Ph.D. in Computer Science from the University of California, Los Angeles, M.S. in Electronic Engineering from the Philips International Institute, the Netherlands, and B.S. in Electronics from the Chinese University of Hong Kong. Dr. Tso is a member of the Robotics Modeling, Simulation, and Visualization Group at JPL. He has worked on a variety of robotics research projects including the JPL Telerobot, Remote Surface Inspection, Web Interface for Telescience, and Lunar Surface Operations Testbed. He is currently the software lead of the GEMS Payload Testbed. His research interests include visualization and simulation, robotics, cyber security, high performance and dependable real-time software and systems.*

Christopher Assad *is a Senior Member of the Technical Staff in the Advanced Robotic Controls group at NASA's Jet Propulsion Laboratory. He received B.S. and Ph.D. degrees in electrical engineering from the California Institute of Technology, in 1987 and 1997 respectively.*

Jaret Matthews *is a senior engineer in JPL's Mobility & Robotics Section, which he joined in 2003. He was responsible for the mechanical design, fabrication, and assembly of the LSOT robotic arm, camera mast, lander mockup, and other testbed elements. He is presently serving as a mobility systems engineer for the Mars Science Laboratory rover that will be launched in November. He recently served as principal investigator for the JPL/Michelin Lunar Wheel and as manager/lead engineer for the ATHLETE lunar rover project. Jaret received the 2011 NASA Exceptional Achievement Medal for his work on ATHLETE. He holds a BS in Aeronautics and Astronautics from Purdue University and a MS from the International Space University. His primary interests are in the design and testing of planetary mobility and manipulation system concepts.*

Robert G. Deen *received a B.S. degree (with honors) in computer science from Texas A&M University (College Station) in 1987. Since then he has worked at the Multimission Image Processing Laboratory of the Jet Propulsion Laboratory in Pasadena, CA, where he is a Principal Software Engineer. His primary duties include responsibility for the ground-based image processing software used for in-situ mission operations and science, including the Mars Exploration Rovers (MER), Phoenix, and Mars Science Laboratory (MSL).*

Douglass A Alexander *is a team leader and system engineer in the Multimisison Instrument Processing Lab at NASA Jet Propulsion Laboratory, California Institute of Technology, where he has been since 1983. He received his B.A. degree in physical geography from the University of California at Santa Barbara in 1980. Mr. Alexander received a 1998 Award for Technical Excellence from JPL for contributions to the Mars Pathfinder mission, and 2004 Outstanding Achievement award for contributions to the Mars Exploration Rover mission.*

Risaku Toda *(Member, IEEE) received a B.S. degree in Applied Physics and a Ph.D. degree in mechatronics and precision engineering from Tohoku University, Sendai Japan. He also received a M.S. degree in materials science and engineering from University of California Los Angeles (UCLA). Prior to joining Jet Propulsion Laboratory, he worked for Ford Motor Company Japan Ltd. and Ball Semiconductor Inc. in Allen TX. Since 2003, he has been with Nano and Micro Systems group at NASA Jet Propulsion Laboratory. His research interests include fabrication of MEMS sensors, actuators and nanotechnology devices for aerospace applications. He holds several US patents.*

Harish M. Manohara (M'07) *received the Bachelor of Engineering degree in instrumentation technology from the Bangalore University, India in 1989, followed by an M.S. degree in nuclear engineering in 1992, and a Ph.D. degree in engineering science in 1997 from the Louisiana State University, Baton Rouge, Louisiana. He joined the Center for Advanced Microstructures and Devices (CAMD) at the Louisiana State University as a Research Associate in January of 1997. In 1998, he became the Assistant Professor of Research at CAMD, and an Adjunct Faculty Member of the Department of Electrical Engineering. While at CAMD, he developed new X-ray microfabrication techniques. In November of 2000 he joined the Jet Propulsion Laboratory to develop advanced silicon and vacuum electronic devices for THz applications. Since 2005, he has been leading the Nano and Micro Systems (NAMS) group at JPL and has developed carbon nanotube field emitters, nanoelectronic devices, miniature spectroscopic instruments, and MEMS for space, defense, medical, and commercial applications.*

Mohammad Mojarradi (SMIEEE) *is a Principal at Jet Propulsion Laboratory in Pasadena, CA. A Senior Member of IEEE, he was the chair of the IEEE San Fernando Valley Section and an integrated circuit design specialist. Specifically he is an expert in developing mixed-signal/mixed-voltage electronic circuits for smart power systems, sensors and micromachined electromechanical interface applications. He leads a consortium of universities developing electronics for extreme environments and manages the development of the electronic circuits for the "thermal cycle resistant electronics" task for Mars Science Laboratory. He also has an on-going collaborative effort on developing smart power integrated mixed-signal electronics for sensors, actuators, and power management and distribution systems. Dr. Mojarradi has over 20 years of technical, management and academic experience. He received his Ph.D. in electrical engineering from the University of California, Los Angeles (UCLA) in 1986. He has twenty-two patents, forty publications and is a member of IEEE. Prior to joining Jet Propulsion Laboratory, Pasadena, CA, he was an Associate Professor at Washington State University and the Manager of the mixed-voltage/specialty integrated circuit group at the Xerox Microelectronics Center, El Segundo, CA.*

Michael T. Wolf *is a research scientist in the Advanced Robotics Controls group at the NASA Jet Propulsion Laboratory, California Institute of Technology. His current work includes probabilistic estimation and classification, human–robot control systems, and biological signal interpretation. Dr. Wolf earned his MS and PhD in the robotics laboratory at Caltech, where his work on neuronal signal tracking for brain–machine interfaces was awarded the Best Thesis in Mechanical Engineering. He received his B.S. in mechanical engineering from Stanford University.*
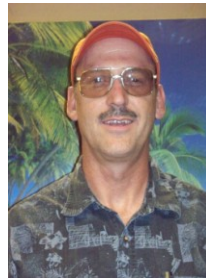
John Wright *has been one of the rover planners for the Mars Exploration Rover missions since landing in January 2004. In this role, his duties include planning all articulated operations of the rover, including mobility and arm operations, on a daily basis. In addition, he is also one of the developers of the Rover Sequencing and Visualization Program used for building command sequences for the rovers and for simulating and visualizing rover activities. Prior to the MER mission, he worked on a variety of tasks involving visualization technology for other missions and non-NASA tasks. He is also currently involved in adapting the visualization tools for use with the upcoming Mars Science Laboratory mission and the ATHLETE robot. Prior to joining JPL in 1994, John worked for over 9 years at Hughes Aircraft Co. on computer graphics algorithms for flight simulator applications. He holds a B.S. in Chemical Engineering from Purdue University and an M.S. in Computer Science from Wright State University.*

Jeng Yen *is one of the developers of RSVP at the Jet Propulsion Lab and is currently one of the rover planners for the MER rovers. Dr. Yen received his PhD in Applied Mathematics with minor in Mechanical Engineering from The University of Iowa at 1990.*

Frank Hartman *received a B.F.A. In Sculpture from the Philadelphia College of Art in 1992. He began employment at the Jet Propulsion Laboratory in 1994 working in the area of computer graphics. After developing three dimensional computer graphics to assist in driving the first Mars rover Sojourner, Frank returned to school and received an M.S. in Aeronautical and Astronautical Engineering from Stanford University in 1999. Frank has been driving the Mars rover Opportunity since its landing in 2004 and is continuing to develop visual simulation applications for controlling planetary robots including the upcoming Mars Science Laboratory mission.*

Robert G Bonitz *is a principal engineer with the Mobility and Manipulation Group at the Jet Propulsion Laboratory. He was the Phoenix Lander 2007 Robotic Arm Manager. Previously he developed the control algorithms and software for the Mars Exploration Rover and Mars Polar Lander robotic arms. He has conducted research in control algorithms for multiple-manipulator robotic systems, robust internal force-based impedance controllers, frameworks for general force decomposition, optimal force control algorithms, and calibration methods for multi-arm robotic systems. He has worked for a variety of industrial companies including Raytheon, TRW, Source 2 International, and GTE. He has a Ph.D. in Electrical Engineering from the University of California, Davis.*

Allen R Sirota *is the technical group supervisor of the Robotic Actuation and Sensing Group at NASA Jet Propulsion Laboratory, California Institute of Technology, where he has been since 1983. He received his B.S. degree in Electronics Engineering from the University of California, Los Angeles, in 1976. Allen Sirota received the 1997 NASA Exceptional Engineering Achievement Medal for his contributions to the Mars Pathfinder Sojourner Rover mission.*
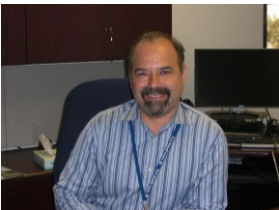
Leon Alkalai , (Member of IAA)*, is the Program Manager of the JPL Lunar Robotic Exploration Program Office in the Solar System Exploration Directorate (4x) and the Capture Lead for the Mars GEophysical Monitoring Stations (GEMS) proposal to the NASA Science Mission Directorate (SMD) Discovery Program which was recently selected for a Phase A study.*

For the last seven years, he has led JPL's lunar robotics mission formulation efforts for both SMD and ESMD, including the Gravity Recovery And Interior Laboratory (GRAIL) mission which won the last Discovery Program competition. Leon was also the formulation lead for the MoonRise Lunar Sample Return mission from the South Pole-Aitken Basin, Phase A study. Prior to transitioning his career at JPL to mission formulation, he worked at JPL for 14 years in the technology development and technology management areas including the Center Lead for the Center for Integrated Space Microsystems. Leon received his PhD from UCLA in 1989 and since then has worked at JPL. He is an Adjunct Faculty at UCLA Computer Science Department, a Full Member for the International Academy of Astronautics (IAA), and the Chief Technologist for the National Space Biomedical Research Institute (NSBRI).